

## Generation of intense uv radiation by subharmonically seeded single-pass free-electron lasers

L. H. Yu

*National Synchrotron Light Source, Brookhaven National Laboratory, Upton, New York 11973*

(Received 1 April 1991)

We present a detailed analysis of a subharmonically seeded single-pass free-electron laser (FEL) utilizing two wiggler magnets separated by a dispersion section. To be specific, suppose the seed to be laser light at 300 nm. A first wiggler is used to energy modulate the electron beam. This is followed by a dispersion section to produce spatial bunching, and a second wiggler resonant to 100 nm. Upon passing through the second wiggler, the prebunched electron beam first radiates coherently, and then this radiation is exponentially amplified. Finally, a tapered section is used to extract additional power from the electron beam. In this manner we can achieve pulses of duration  $\approx 10$  psec with 1 mJ per pulse in  $10^{-4}$  bandwidth, with continuously tunable wavelength in the range 100–300 nm. We present the analytical tools we have employed for the preliminary estimate of the system performance and of the optimization of the parameters. We describe our modification of the simulation code TDA to include harmonic generation and discuss its use in analyzing the subharmonically seeded FEL. The analytic and computer-simulation calculations are in good agreement. We discuss in detail the physical process in the system and the optimization of parameters.

PACS number(s): 42.55.Tb

### I. INTRODUCTION

The development of a high-power uv free-electron laser (FEL) operating in the wavelength range from 300 to 100 nm or shorter could have a significant impact on experimental studies of photoinduced processes in chemistry, physics, and biology [1]. The design of such a device using an input seed laser and a FEL amplifier was recently discussed [2]. Here we present an analysis of a subharmonically seeded single-pass FEL utilizing two wiggler magnets separated by a dispersion section (see Fig. 1, Scheme 2). To be specific, suppose the seed to be laser light at 300 nm. A first wiggler is used to energy modulate the electron beam. This is followed by a dispersion section to produce spatial bunching, and a second wiggler resonant to 100 nm. Upon passing through the second wiggler the prebunched electron beam first radiates coherently, and then this radiation is exponentially amplified. Finally, a tapered section is used to extract additional power from the electron beam. In this manner we can achieve pulses of duration  $\approx 10$  psec with 1 mJ per pulse in  $10^{-4}$  bandwidth, with continuously tunable wavelength in the range 100–300 nm.

We assume an electron pulse of 250 MeV and length 15 ps from a linear accelerator with a laser-driven photocathode rf gun. The electron beam has a peak current of 300 A, normalized emittance (rms) 8 mm mrad, local energy spread 0.1% full width at half maximum (FWHM), and global energy spread 0.3%. This set of electron-beam parameters (see Table I, column 3) has been realized in the recent Los Alamos high brightness injector experiment except that the beam energy was only 15 MeV [3]. In Sec. II B we will explain the concept of the local energy spread, and show that the assumed 0.1% local energy spread is a conservative estimate.

The FEL consists of an initial 2-m-long wiggler reso-

nant to 300 nm, a dispersion section of length 20 cm, 2.8-kG magnetic field, and a second wiggler resonant to 100 nm of length 11 m. The interaction of the 300-nm and 4.2-MW seed pulse with the electron beam produces an energy modulation at 300 nm. This energy modulation is converted into a spatial bunching with a strong third-harmonic component at 100 nm in the dispersion section. When the coherently bunched beam enters the second wiggler magnet, there is a rapid coherent generation of 100-nm radiation within the first meter, and the radiation has a characteristic quadratic dependence on distance traversed in the wiggler. There is then a transition to exponential growth which continues until 7 m into the wiggler where the 100-nm radiation approaches saturation. At this point the tapering and large energy extraction from the electron beam into the radiation begin. The distinct three different stages in the second wiggler (the quadratic “superradiance” growth, the exponential growth, and the quadratic growth in the tapered section) are shown clearly when the radiation power plotted against the wiggler length in Fig. 2.

In this paper, we discuss the detailed analysis of the physical processes in the different sections of this device, the analytical and numerical calculation, and the parameter optimization.

The idea of using two wigglers, with the second wiggler resonant to one of the harmonics of the first, has been proposed by Bonifacio *et al.* to generate uv radiation at the several megawatt level [4]. In their approach, the first wiggler is long enough to reach saturation and produce strong spatial bunching, which is rich in harmonics. The second wiggler immediately follows the first, using the bunched beam to generate coherent superradiation. This radiation reaches saturation at a few megawatts at about 2 m into the second wiggler. We introduce the following modifications.

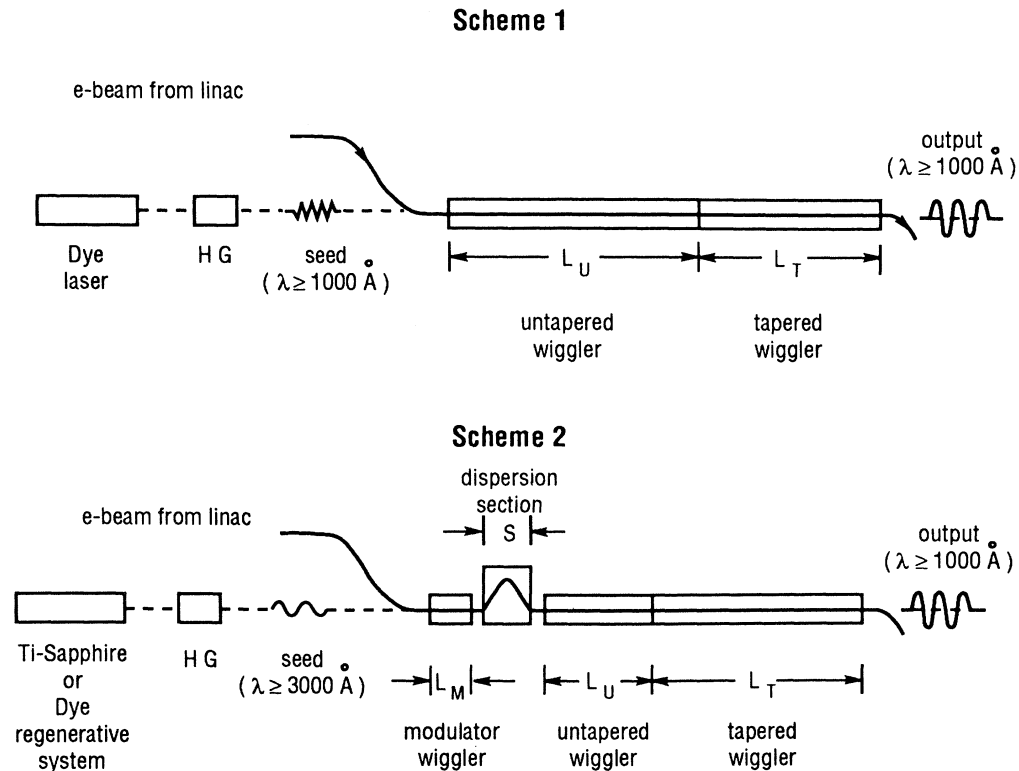


FIG. 1. Two seeded single-pass FEL schemes. (HG represents harmonic generation.)

(i) We significantly shorten the first wiggler, and control the input laser power so that the maximum energy modulation is about equal to the energy spread, but still far away from saturation.

(ii) We introduce a dispersion section between the two

wigglers, and optimize the dispersion strength to generate maximum harmonics in the spatial bunching as in a transverse optical klystron [5].

(iii) We extend the second wiggler so that there is an exponential growth after the initial superradiation. This

TABLE I. FEL parameters at 100 nm. The asterisk denotes second wiggler in harmonic generation cases.

	uv seed	Harmonic generation	Harmonic generation
Input seed wavelength (nm)	100	300	300
Input seed power (MW)	0.0007	1.5	4.2
Electron beam energy $\gamma$	503	503	490
Current (A)	100	100	300
Normalized rms emittance (mm mrad)	6	6	8
FWHM local energy spread (%)	0.1	0.1	0.1
FWHM global energy detuning range (%)	0.18	0.2	0.25
Dispersion $d\theta/d\gamma$		0.33	0.83
$\rho$ in the exponential section* ( $\times 10^{-3}$ )	1.29	1.29	1.53
Period of the first wiggler (cm)	1.75	2.8	3.5
Period of the second wiggler (cm)		1.75	2.2
Magnetic field of the first wiggler (T)	1.19	1.14	0.76
Magnetic field of the second wiggler (T)		1.19	0.75
Magnetic gap of the wiggler (mm)	4	4	6
Length of untapered section* (m)	11	8	7
Length of tapered section* (m)	10	12	4
Tapering* (%)	1.8	1.6	1.2
Output radiated power (MW)	160	100	155
Electron pulse length (psec)	6	6	10
Output radiation energy per pulse (mJ)	1	0.6	1.6

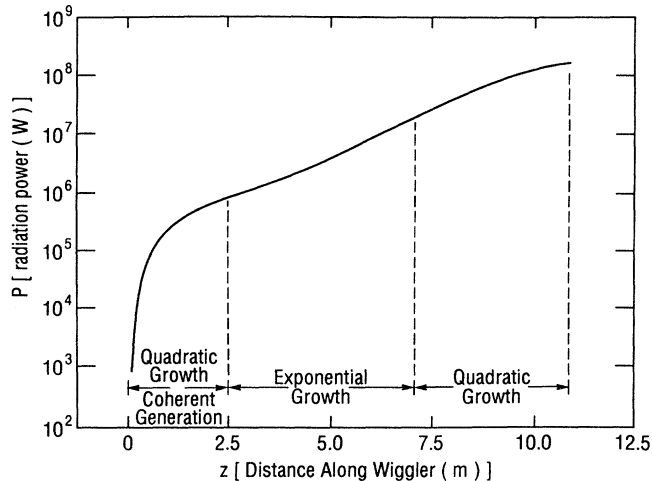


FIG. 2. Radiation power vs distance in the second wiggler of the 300-nm seeded FEL for LANL gun parameters.

is possible because of the proper control of the energy modulation in the first wiggler. If the energy modulation is too small, the harmonic component in the spatial bunching after the dispersion section is too small even when the dispersion strength is optimized. If the energy modulation is too large, on the other hand, it behaves as an equivalent energy spread in the second wiggler, and saturation is reached too early, without achieving exponential growth after the superradiance section. In addition, the number of electrons trapped in the bucket in the tapered section is reduced, and energy extraction efficiency drops.

(iv) At the end of the exponential section, near but before saturation, we start tapering the magnetic field. This allows a much larger energy extraction, which is necessary to achieve the level of hundreds of megawatts at the end of the tapered section.

Before we selected this subharmonically seeded single-pass FEL, we considered other configurations, starting from the oscillator configuration. In the case of an oscillator, it is difficult to achieve output power of the same level as the radiation power inside the cavity because there is no  $Q$  switch in this wavelength range to carry out a cavity dump. Hence the output can only be realized by output coupling. Therefore, to achieve output power in the level of hundreds of megawatt, the inside cavity radiation power should be much higher, giving very stringent requirements on the mirror damage threshold for the cavity. To avoid this difficulty, we considered the master oscillator power amplifier configuration [6]. The result of our estimate was that the sum of the wiggler lengths inside and outside the cavity would be 17 m in order to achieve the radiation power of 1 mJ within 3 ps, using a set of electron-beam parameters based upon an earlier Advanced Test Facility (ATF) gun design at Brookhaven National Laboratory (BNL) (see Table I, column 1).

The oscillator configuration requires an electron-beam time structure with each macropulse comprised of a train

of hundreds of micropulses. To satisfy the output frequency stability requirement, which is critically important for a user facility, this configuration requires very high energy stability between micropulses. This leads us to consider instead the seeded single-pass FEL as shown in Fig. 1 (Scheme 1). Using harmonic generation from a conventional laser by nonlinear media (e.g., gas cell), it is possible to achieve continuously tunable uv radiation of a few hundred watts with a pulse length of a few picoseconds [2]. This seed is amplified in an exponential growth section to near saturation before tapering. We used an analytical tool developed recently to analyze this process. The growth rate in the exponential section was calculated in terms of a universal scaling gain function, which incorporated the energy spread, emittance, the focusing of the electron beam, and the diffraction and guiding of the radiation [7]. The high speed of this method made it particularly easy to optimize the parameters for the wiggler and the electron beam. The estimate on the start-up, the saturation, and the tapering are based on a one-dimensional analysis. Our analytical estimate using the ATF gun parameters and optimized wiggler parameters give the total wiggler length as 21 m to achieve the 1-mJ radiation energy for a 3-ps pulse. This estimate of the output power, even though only a crude one, was later found to agree with numerical simulation within about 30% using a code TDA provided by Tran and Wurtele [8].

The required wiggler length is comparable with that required for the oscillator configuration. However, the seeded single-pass FEL has many advantages. The output bandwidth is controlled by the input seed and is only limited by the pulse length, and hence it is possible to achieve a bandwidth of  $10^{-4}$ . Similarly, the frequency stability is also controlled by the seed, hence the electron-beam energy stability only influences the output intensity fluctuation, and the requirement on the energy stability is largely relaxed. Another evident advantage is that the mirror damage problem is eliminated. In addition, there is no need for a long train of micropulses; the electron beam could be made of individual micropulses with very high repetition rate, as can be achieved by a superconducting linear accelerator. Thus it is possible to achieve very good energy stability and high average power.

Next, we proceeded to consider the possibility of using a 300-nm seed instead of 100 nm, because it is much easier to tune at this wavelength. This is the subharmonically seeded scheme illustrated in Fig. 1 (Scheme 2), mentioned earlier. For the ATF gun parameters, we optimized both the 100-nm seeded and 300-nm subharmonically seeded cases. In Fig. 3, we plotted the radiation power versus distance along the wiggler for both cases. This plot shows that, at first, the subharmonically seeded scheme gives much larger output power because of the initial fast generation of coherent radiation. However, since the energy modulation produces an effective energy spread, its growth rate in the exponential section is lower, and finally the power of the 100-nm seed scheme surpasses it.

The calculation was carried out by modifying the code

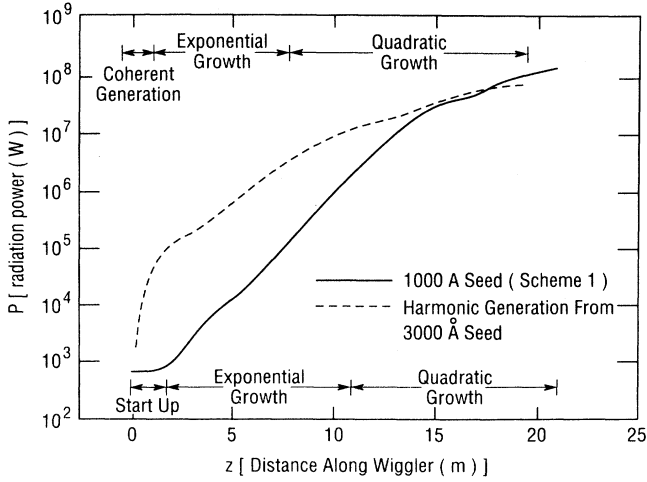


FIG. 3. Radiation power vs distance for both 100- and 300-nm seeds and ATF gun parameters.

TDA to include harmonic generation. The modification has been checked by an analytical calculation, developed for a one-dimensional model in the small energy spread limit.

These simulation results have been reported in Paris [2]. We obtained the new Los Alamos National Laboratory (LANL) gun parameters, based on which we optimized our design parameters again. The results show that since the new parameters have much higher current and longer pulse, the radiation power for the subharmonically seeded case reaches the required level before the 100-nm seeded scheme catches up. Therefore the subharmonically seeded single-pass FEL is far superior for the new LANL gun parameters, requiring a much shorter wiggler length to achieve 1-mJ output. In addition to this, the subharmonically seeded approach provides the possibility of obtaining output at wavelengths shorter than 100 nm.

This paper is organized as follows. In Sec. II, we describe our modification of the simulation code TDA to include harmonic generation from a 300-nm seed. We then compare it with the simulation for the 100-nm seed. Next, in Sec. III, we describe an analytical one-dimensional model for the subharmonically seeded single-pass FEL in the small energy spread limit. This has been used to check our modified version of Tran and Wurtele's TDA code. It also sheds some light, in a more quantitative way, on why the energy modulation in the first wiggler should be about equal to the energy spread. Finally, in Sec. IV, we conclude with a description of our parameter optimization for the new LANL gun parameters.

## II. NUMERICAL SIMULATION AND THE SYSTEM PARAMETERS

### A. The code TDA

Our calculation is carried out by modifying the simulation code TDA, provided by Tran and Wurtele [8]. In this

code, the electron motion is described three dimensionally and the radiation field is assumed to be axially symmetric.

The longitudinal motion is governed by the following equations for the Lorentz factor  $\gamma$  and the electron phase  $\theta = (k_s + k_w)z - \omega_s t$ :

$$\frac{d\gamma}{dz} = -\frac{k_s a_w a_s [JJ]}{\gamma} \sin(\theta + \phi_s), \quad (2.1)$$

$$\frac{d\theta}{dz} = k_w - k_s \frac{1 + a_w^2 + p_x^2 + p_y^2 + 2a_w a_s [JJ] \cos(\theta + \phi_s)}{2\gamma^2}. \quad (2.2)$$

In these equations, the radiation field is characterized by the wave number  $k_s = 2\pi/\lambda_s = \omega_s/c$ , the dimensionless vector potential rms value  $a_s = eA_s/mc$ , and phase  $\phi_s$ , while the wiggler field is specified by the wave number  $k_w = 2\pi/\lambda_w$  and dimensionless vector potential rms value  $a_w = eB_w/(\sqrt{2}mk_w)$ . For planar wiggler, the Bessel factor  $[JJ]$  is given by

$$[JJ] = J_0 \left[ \frac{a_w^2}{2(1+a_w^2)} \right] - J_1 \left[ \frac{a_w^2}{2(1+a_w^2)} \right]. \quad (2.3)$$

For helical wiggler  $[JJ] = 1$ . In Eq. (2.2),  $p_x$  and  $p_y$  are the transverse momentum normalized by  $mc$ , averaged over a wiggler period to cancel out the fast wiggle oscillations. They evolve according to

$$\frac{dp_x}{dz} = -\frac{1}{2\gamma} \frac{\partial}{\partial x} a_w^2, \quad (2.4)$$

$$\frac{dp_y}{dz} = -\frac{1}{2\gamma} \frac{\partial}{\partial y} a_w^2, \quad (2.5)$$

where the wiggler field  $a_w$  has a transverse profile

$$a_w = a_{w0} \left[ 1 + \frac{1}{4} k_w^2 (x^2 + y^2) \right] \quad (2.6)$$

because we assume our wiggler is a planar wiggler with the pole faces shaped to produce equal focusing in both horizontal and vertical planes [9]. The equations for the averaged transverse position are

$$\frac{dx}{dz} = \frac{p_x}{\gamma}, \quad (2.7)$$

$$\frac{dy}{dz} = \frac{p_y}{\gamma}. \quad (2.8)$$

These single-particle equations of motion are coupled to the Maxwell equations written in terms of the slowly varying amplitude and phase and assuming a single frequency and the paraxial approximation:

$$\left[ \frac{\partial}{\partial z} + \frac{1}{2ik_s} \nabla^2 \right] a_s e^{i\phi_s} = i \frac{eZ_0 [JJ] I_0}{mc^2 2k_s N} \times \sum_{j=1}^N \delta(x-x_j) \delta(y-y_j) a_w(x_j, y_j) \frac{e^{-i\theta_j}}{\gamma_j}, \quad (2.9)$$

where  $Z_0=377 \Omega$  is the vacuum impedance. On the right-hand side, each of the  $N$  simulation particles carries the partial current  $I_0/N$ . Since the code assumes axial symmetry,  $a_s$  and  $\phi_s$  are functions of radius  $r=(x^2+y^2)^{1/2}$  only. The TDA code uses the Runge-Kutta method to solve these coupled equations and find the particle position, momentum, and the radiation field, step by step, in the  $z$  direction.

### B. The system parameters

Before discussing our application of the code TDA and its modification to introduce the harmonic generation, let us first consider the electron beam and wiggler parameters. When we compare the 100-nm seed and the 300-nm seed configurations, we use as an example a set of parameters based on the ATF (at BNL) laser-driven photocathode rf gun:  $I_0=100$  A,  $\epsilon_n=6$  mm mrad, and the FWHM energy spread is 0.1%.

Let us discuss a little further the concept of local energy spread which determines the gain in our calculations. During the passage through the whole wiggler (about 1000 wiggler periods) the slippage distance is only 0.1 mm, as compared with the bunch length of 2 mm for a 6-psec pulse. We call the energy spread within this slippage distance the local energy spread. Because the slippage distance is only 0.1 mm, which is much smaller than the size of different parts of the accelerating structures in the linac, there is no mechanism to increase the energy spread within this distance except the quantum nature of the synchrotron radiation, which is negligibly small for electron beams in a linear accelerator. Since the energy spread of the electron gun is about 20 keV, and we do not expect this to be significantly increased in the linac, we believe 0.1% is a conservative estimate for the local energy spread (at 250 MeV, 20-keV energy spread gives the fractional energy spread 0.008%). The global energy spread, including the energy chirp within an electron bunch introduced by the wake field and the curvature of the accelerating gradient in the linear accelerator, and the fluctuation between bunches will be taken into account as a detuning, as will be discussed later. This set of parameters is conservatively selected to have less current than the ATF gun design current (160 A).

The total length of the wiggler is mainly determined by the power gain length  $L_G$  (the length of the wiggler for the radiation power to increase by a factor  $e$ ). Therefore the selection of the system parameters should start from the gain length calculation. The analytical tool we developed for the rapid gain calculation [7] is particularly convenient in the optimization procedure. Our analysis gives a universal scaling gain function for the exponential growth regime. This method takes into account the energy spread, emittance, and focusing of the electron beam, and the diffraction and optical guiding. The water-bag transverse electron distribution we use in the calculation is a model widely used in many simulation codes, including TDA. For a detailed description of this model and the solution for gain length, and the parameter optimization, we refer to Ref. [7]. For a complete design report, other transverse distributions (e.g., Gaussian distribution) or

even a specific distribution calculated by a complete simulation of the electron gun and the linear accelerator should also be considered. Our simulation for the exponential growth section shows that the waterbag model and the Gaussian model do not give significantly different results. For simplicity, in this paper we concentrate on the water-bag model, which is easy to check against analytical solution.

The water-bag distribution has a uniform longitudinal density, and a uniform distribution inside a four-dimensional sphere in the four-dimensional transverse phase space  $\mathbf{R}=(x,y)$ ,  $\mathbf{R}'=d\mathbf{R}/dz=(x',y')$ . The transverse electron density has a parabolic profile within the edge beam size  $R_0$ . Outside  $R_0$ , the density is zero. The electron beam's energy distribution is Gaussian, with average energy  $\gamma_0 mc^2$  and rms spread  $\gamma_0 \sigma$ .

The static wiggler magnetic field has period length  $\lambda_w$  and wave number  $k_w=2\pi/\lambda_w$ . The resonant radiation frequency  $\omega_s=k_s c$  of the FEL is determined by  $k_s=2\gamma_0^2 k_w/(1+a_w^2)$ , where  $a_w=eB_w/(\sqrt{2}k_w mc)$  and  $B_w$  is the peak on axis magnetic field. We assume a planar wiggler with parabolic pole faces providing equal natural focusing on both vertical and horizontal plane with the betatron wave number  $k_\beta=a_w k_w/(\sqrt{2}\gamma)$  [9]. When the electron beam is matched to the natural focusing, the beam distribution remains invariant, and the edge beam radius  $R_0$  is related to the rms emittance  $\epsilon$  by

$$\epsilon=(\langle x^2 \rangle \langle x'^2 \rangle)^{1/2}=(\langle y^2 \rangle \langle y'^2 \rangle)^{1/2}=k_\beta R_0^2/6. \quad (2.10)$$

Our theory shows that the power gain length  $L_G$  can be expressed in a scaled form. The scaled growth rate  $1/(2k_w L_G D)$  is a function of the ratio of emittance over wavelength  $k_s \epsilon$ , the scaled energy spread  $\sigma/D$ , the scaled focusing strength  $k_\beta/(k_w D)$ , and the scaled detuning  $(\omega-\omega_s)/(\omega_s D)$ :

$$\frac{1}{2k_w L_G D}=G\left[k_s \epsilon, \frac{\sigma}{D}, \frac{k_\beta}{k_w D}, \frac{\omega-\omega_s}{\omega_s D}\right], \quad (2.11)$$

where  $D$  is the scaling parameter (a measure of transverse current):

$$D=\left[\frac{4eZ_0}{\pi mc^2} \frac{a_w^2}{1+a_w^2} \frac{I_0}{\gamma_0}\right]^{1/2} [JJ], \quad (2.12)$$

with  $[JJ]$  defined by Eq. (2.3).

The function  $G$  can be calculated by solving two coupled equations using Newton's root finding routines. The results have been checked against the simulation codes FELEX [10] and FRED [11] for several cases, and yield agreement to within 5%. For maximum gain, the detuning can be chosen to be

$$\frac{\omega-\omega_s}{\omega_s D}=-3\left[\frac{k_\beta}{k_w D}\right] k_s \epsilon, \quad (2.13)$$

which we found to yield near-maximum gain.

Let us now consider the optimization. The required radiation wavelength  $\lambda_s$  is specified as 100 nm, and we are given the set of electron-beam parameters: the current  $I_0=100$  A, the normalized emittance  $\epsilon_n=\epsilon\gamma=6$

mm mrad, and the fractional FWHM energy spread 0.1%. If we select a wiggler period  $\lambda_w$  and an on-axis magnetic field  $B_w$ , the wiggler parameter  $a_w$  would be determined, and through the resonance condition the electron-beam energy would also be determined. Following this, the emittance  $\epsilon$ , the betatron wave number  $k_\beta$ , the scaling parameter  $D$ , and the optimum detuning can all be calculated. Now all these parameters can be substituted into the gain function  $G$  to obtain the gain length  $L_G$ .

For a given wiggler type, there is a relation between the wiggler period  $\lambda_w$  and wiggler field  $B_w$ . For example, we assume the wiggler to be of design with Nd-Fe-B magnet blocks and vanadium-Permendur pole tips. The magnetic field is related to  $g/\lambda_w$  (the gap-to-period ratio) by Halbach's relation [12] ( $g/\lambda_w \leq 0.722$ )

$$B_w = 3.44 \exp[-5.00(g/\lambda_w) + 1.54(g/\lambda_w)^2]. \quad (2.14)$$

Therefore once the gap  $g$  is fixed, we can consider the gain length as a function of the wiggler period  $\lambda_w$ , and minimize it using our rapid calculation method. When we fix the wiggler gap at 4 mm, the gain length as a function of the wiggler period is plotted in Fig. 4, giving the minimum gain length  $L_G = 1.1$  m at  $\lambda_w = 1.75$  cm, with electron-beam energy 250 MeV, edge beam radius 0.3 mm, the wiggler peak-on-axis field 1.19 T, and  $a_w = 1.37$ . This result is compared with numerical simulation in Fig. 5. The radiation power gain in logarithmic scale, as a function of the wiggler distance, is shown as a straight line. The slope of the straight line gives the gain length 1.1 m, in agreement with the analytical result. The straight line intersects with the vertical axis at a point determined by the coupling between the input laser beam and the electron beam. This is because there is a lethargy distance [13] before the radiation starts to grow exponentially, as can be seen in Fig. 5.

Next, we consider the effect of the global energy spread. If the global energy spread is within an electron bunch, as induced by wake field or the curvature of the accelerating field, its effect is that a part of the electron

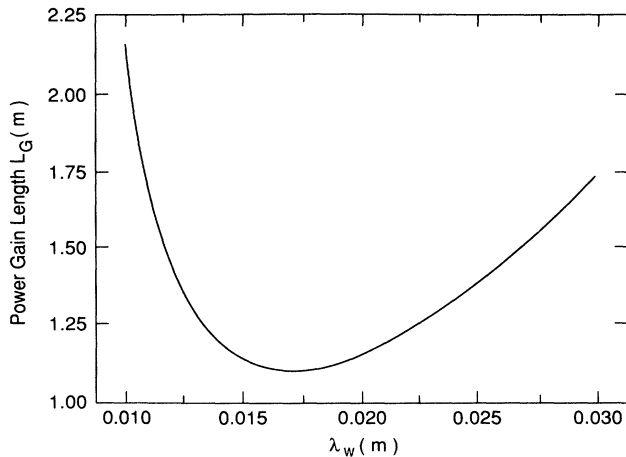


FIG. 4. Power gain length as a function of wiggler period for ATF gun parameters.

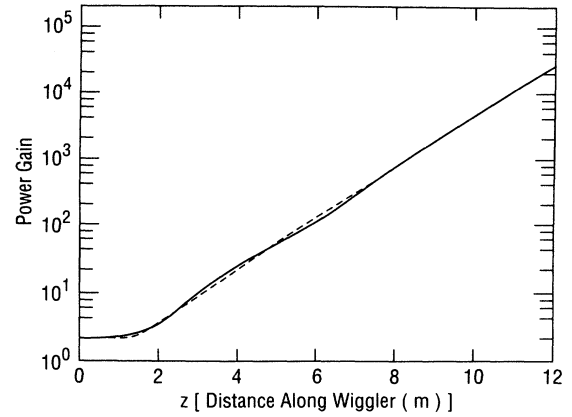


FIG. 5. Radiation power vs distance for a 100-nm seeded FEL with ATF gun parameters. This plot is used to calculate the gain length from the simulation and to test with the analytical result.

bunch with energy outside a certain energy detuning bandwidth would contribute little to the output. On the other hand, if the energy spread is referred to the energy fluctuation between bunches, and if the energy spread within a bunch is smaller than the bandwidth, the effect would be an intensity fluctuation from pulse to pulse. The average electron-beam energy is selected to have the maximum gain at the input laser frequency. If the electron-beam energy deviates from this average energy, the wavelength for the maximum gain would shift away from the input laser frequency, corresponding to a detuning reducing the gain. When the deviation is within  $\pm 0.12\%$ , the gain length varies between 1.1 and 1.4 m. If we select 1.4 m as the gain length to design the system, the energy detuning bandwidth would be 0.24%.

### C. Direct amplification of the 100-nm seed

Let us first consider the case of the uv seed at 100 nm. The FEL amplifier is comprised of a 21-m constant period wiggler. The magnetic field is constant over the first 11 m and the amplification in this section is exponential. The magnetic field is tapered quadratically over the last 10 m,

$$B_w = B_{w0} \left[ 1 - \eta \left( \frac{z - 11}{10} \right)^2 \right], \quad (2.15)$$

with  $\eta = 0.018$ , yielding an approximately quadratic power growth. A simple analytical estimate shows that the quadratic tapering gives the optimized performance for small energy extraction (less than a few percent of the electron-beam energy). Our simulation tested many different types of tapering, and confirmed this conclusion. For simplicity, we will not elaborate on this.

We optimized the position of the beginning of the tapered section and the tapering coefficient  $\eta$  by individually varying these quantities to find the maximum output power. The input seed pulse at 100 nm has a pulse length of 6 psec and an energy of 4 nJ corresponding to a peak

power of 700 W, in a bandwidth  $\Delta\lambda/\lambda=10^{-4}$ . We assume the laser beam is Gaussian, the beam waist is equal to the electron-beam size, and coincides with it at the entrance of the wiggler. In the exponential section, the power gain length is 1.1 m, and the amplified power after 11 m has reached 3.2 MW, which is near but before saturation of the exponential process. In the 10-m tapered section, the power is increased from the initial 3.2 MW to an output value of 160 MW. The exponential growth in the untapered section and the nearly quadratic growth in the tapered section are shown in Fig. 3.

These results have been checked against an one-dimensional estimate of saturation of the exponential section and the output power of the tapered section (see Appendix B). Our estimate predicts the starting position of tapering to be at 11.7 m, with saturation power of 3.2 MW, and the output power of 210 MW at the end of the tapered section, in good agreement with the simulation, considering the approximate nature of the estimate.

#### D. Modification of the code TDA to include harmonic generation

Now let us consider the subharmonically seeded FEL process. The 300-nm seed laser light interacts with the electron beam in the first wiggler resonant to 300 nm, being amplified by a factor of about 1.4, and produces an energy modulation in the electron beam with amplitude about equal to the rms energy spread. The modulated electron beam then passes through the dispersion section, where the electron energy modulation is converted into a spatial microbunching. With proper choice of the input laser power and dispersion section parameters the spatial density will have significant harmonic components. This bunched beam, when traversing the second wiggler resonant to 100 nm, produces coherent 100-nm radiation. It experiences a rapid power growth within a few meters, where it is comprised of many modes; some are exponentially growing, and some are oscillating or decaying. Then the fundamental guided mode dominates, and the power grows exponentially until 8 m where it approaches saturation and tapering starts. In the tapered section, a significant portion of the electrons are trapped into buckets and form microbunches spaced by 100 nm. These microbunches again radiate coherently, and the power grows quadratically until the exit of the wiggler.

Now we discuss the modifications of the code TDA required to carry out the calculation of the harmonic generation. For the ATF gun parameters, the first wiggler is 2.5 m long and has a period  $\lambda_{w1}=2.8$  cm and a peak magnetic field  $B_{w1}=1.14$  T. The second wiggler has a period  $\lambda_{w2}=1.75$  cm. Its field is  $B_{w2}=1.19$  T over the first 8 m and is tapered according to

$$B_w = 1.19 \left[ 1 - 0.016 \left( \frac{z-8}{12} \right)^2 \right] \quad (2.16)$$

over the last 12 m. The parameters of the second wiggler are the same as those used in the 100-nm seed case. The first wiggler parameters have been selected to be resonant to 300 nm and to yield approximately the same betatron wavelength as the second wiggler, hence the electron-

beam profile remains the same in both the wigglers.

The initial seed pulse at 300 nm has a power of 1.5 MW, and is focused to have a Rayleigh range of 24 cm, with the beam waist located at 24 cm into the entrance of the first wiggler. At the end of the first wiggler, the longitudinal phase space  $(\theta, \gamma)$  distribution is shown in Fig. 6(a). The energy is modulated with the peak to peak value of  $2\Delta\gamma/\gamma \approx 1.6 \times 10^{-3}$ , about equal to the energy spread. We modified the code TDA to output the electron parameters  $x, y, p_x, p_y, \gamma, \theta$  for all the simulation particles into a file to be processed by a simulation of the dispersion section.

In the dispersion section, the parameters  $x, y, p_x, p_y, \gamma$  remain unchanged, but the longitudinal phases of different particles change with the variation proportional to their deviation from the average energy. We assume the idealized dispersion section is divided into three sections with total length  $L_d$ , the field is [14]

$$B(z) = \begin{cases} B_0, & 0 \leq z < \frac{L_d}{4} \\ -B_0, & \frac{L_d}{4} < z < \frac{3L_d}{4} \\ B_0, & \frac{3L_d}{4} < z < L_d \end{cases} \quad (2.17)$$

This configuration satisfies the condition that the first and

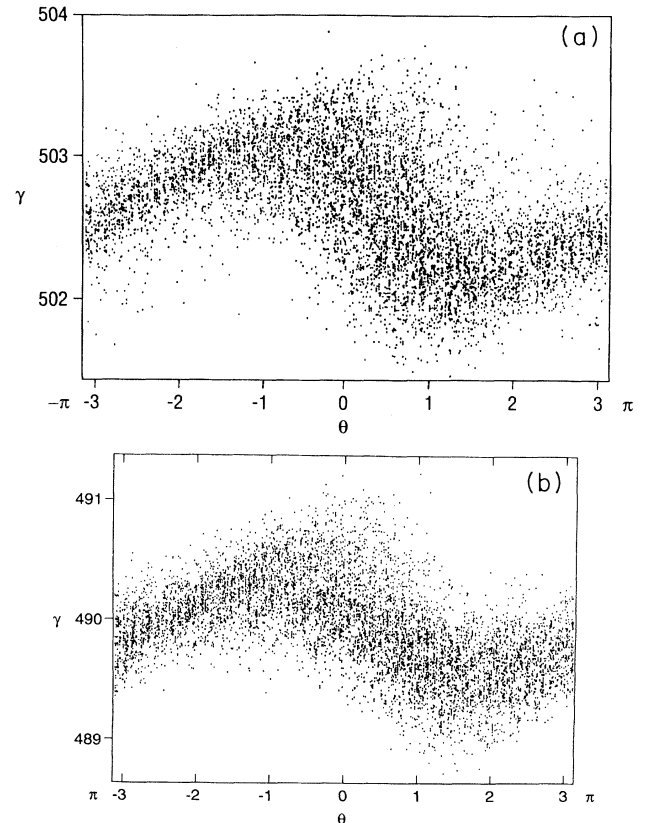


FIG. 6. Phase-space  $(\gamma, \theta)$  distribution at the end of the first wiggler for the 300-nm seeded FEL. (a) is with ATF gun parameters, (b) is with LANL gun parameters.

second integrals over  $z$  of the magnetic field vanish so as to have no transverse and angular displacements. However, the particles with the same longitudinal coordinate  $z$  but different energy have different transit time in the dispersion section. The difference of the transit time is

$$\Delta t = \frac{dt}{d\gamma} \Delta\gamma, \quad (2.18)$$

where  $\Delta\gamma$  is the difference of the particle energy, and

$$\frac{dt}{d\gamma} = -\frac{e^2}{m^2 c^3 \gamma^3} \frac{B_0^2 L_d^3}{48}. \quad (2.19)$$

This relation between transit time and energy converts energy modulation into coherent bunching. Now we will rewrite this time-energy relation as the phase-energy relation at the entrance of the second wiggler. The phase of particle  $j$  at the end of the first wiggler  $z_1$  is

$$\theta_j = (k_{s1} + k_{w1})z_1 - \omega_{s1}t_{j1}, \quad (2.20)$$

where  $t_{j1}$  is the time of arrival. Correspondingly, at the entrance  $z_2$  of the second wiggler the phase is

$$\psi_j = (k_{s2} + k_{w2})z_2 - \omega_{s2}t_{j2}. \quad (2.21)$$

The arrival time  $t_{j2}$  at the second wiggler  $z_2$  is related to  $t_{j1}$  by

$$t_{j2} = t_{j1} + \frac{dt}{d\gamma}(\gamma_j - \gamma_0) + t_0, \quad (2.22)$$

where  $t_0$  is a constant dependent on the position of the second wiggler. From (2.20)–(2.22) we obtain the phase-energy relation in the second wiggler

$$\psi_j = \frac{\omega_{s2}}{\omega_{s1}} \left[ \theta_j + \frac{d\theta}{d\gamma}(\gamma_j - \gamma_0) + \theta_0 \right]. \quad (2.23)$$

We will not write down the specific expression for  $d\theta/d\gamma$  and  $\theta_0$ , but we point out that they are dependent on the length and magnetic field of the dispersion section and the positioning of the second wiggler, but independent of the particle index  $j$ . The ratio  $n \equiv \omega_2/\omega_1$  is equal to the harmonic number 3 in our example. Our simulation gives  $d\theta/d\gamma = 0.33$  as the optimum. For our harmonic-generation scheme the output power is independent of  $\theta_0$ , so we choose  $\theta_0 = 0$ .

After determining the parameter  $\theta$  at the end of the dispersion section for all the particles, parameters  $x, y, p_x, p_y, \gamma, \theta$  for all the particles are written into a file as an input to the simulation of the process in the second wiggler. The phase-space distribution is given in Fig. 7(a), showing the enhancement of the bunching introduced by the dispersion section, compared to Fig. 6(a). This enhancement, for the case with ATF gun parameters, is not very significant, even though it is visible. However, the corresponding figures [Figs. 6(b) and 7(b)], for the LANL gun parameters (see Sec. IV), show a more pronounced enhancement. We modified the code TDA so that, for the second wiggler, these input particle parameters are used as the initial condition (instead of the water-bag model initial distribution used at the beginning of the first wiggler). Since the 100-nm component of the

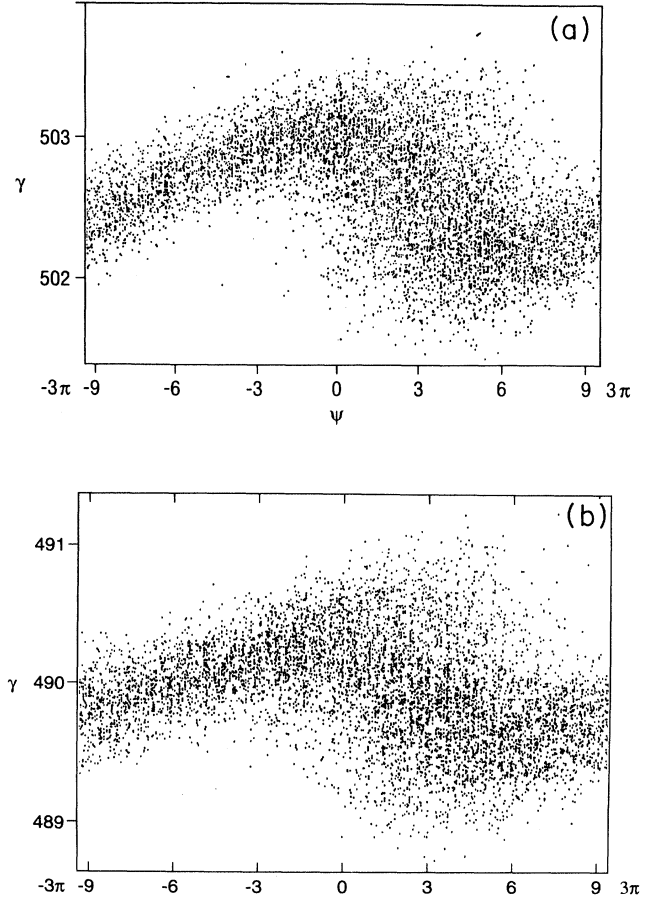


FIG. 7. Phase-space distribution at the entrance of the second wiggler is with (a) ATF gun parameters and (b) LANL gun parameters.

radiation field is generated by coherent microbunching, the initial field  $a_s$  is taken as zero. Another modification relates to the range of the phase  $\theta$ . In the original code, it is modular from  $-\pi$  to  $\pi$ , and when the particle increases past  $\pi$ , the code automatically subtracts  $2\pi$  to keep it within the range. For third-harmonic generation the phase range for the second wiggler must increase by a factor of 3, becoming  $-3\pi$  to  $3\pi$ , as easily seen from (2.23). Physically this means that the electrons distributed in one 300-nm wavelength now occupy three harmonic 100-nm wavelengths. In the second wiggler, even though the fundamental radiation wavelength is 100 nm, the periodicity of the electron distribution is 300 nm.

For the calculation in the second wiggler, we neglect the higher harmonics of 100 nm: 33, 20 nm, etc., because the growth rate is smaller due to the more stringent requirement on the emittance-wavelength ratio and different detuning of maximum gain as given by (2.13). After the exponential growth section in the second wiggler, they are all dominated by the fundamental guided mode at 100 nm. In the tapered section, the microbunching on the 100-nm scale becomes significant. In Fig. 8, we plot the phase-space distribution at the beginning of the tapered section, near saturation of the ex-

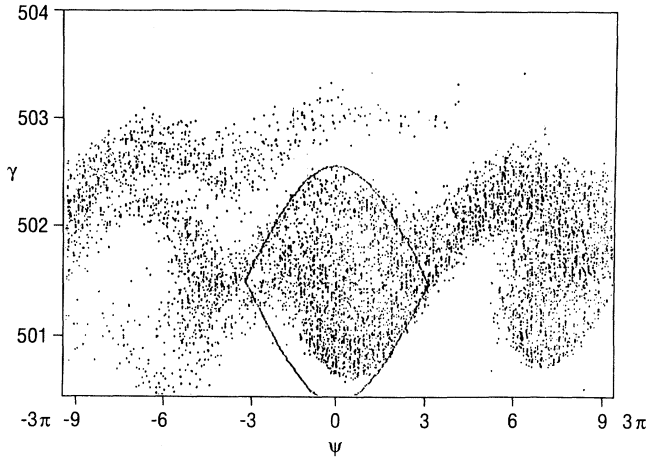


FIG. 8. Phase-space distribution at the beginning of the tapered section.

ponential growth, and we see that the periodicity is still 300 nm, but 100-nm bunching is clearly visible. We also plotted one of the separatrices to show that a significant portion of the particles has been trapped in the bucket. It is rich in harmonics, and there will be coherent spontaneous harmonic radiation. But we expect the intensity of higher harmonics to be much lower than at 100 nm, and should be easily reduced by spatial filtering using the fact that in the output these higher harmonics have smaller angular divergence than the fundamental. We do not expect the existence of these harmonics to influence the accuracy of our calculation of the 100-nm output power.

In Fig. 3, we plot the radiation power versus the distance in the second wiggler. As we pointed out in the Introduction, the process can be seen to be distinctly divided into three stages: the coherent harmonic generation with quadratic growth, the exponential growth, and the energy extraction in the tapered section with quadratic growth again. On the same figure, we also plot the power of the 100-nm seed FEL as a comparison. In the first 2 m, while its coherent bunching is generating a rapid quadratic growth, the 100-nm seeded FEL is still in lethargy. But after 2 m, when it is in exponential regime, the slope in the case of harmonic generation is smaller than the other because there is an effective energy spread introduced by the energy modulation in the first wiggler. As a result, the harmonically generated power grows slower, and at about 18 m, it is passed by the 100-nm seeded FEL. Finally, at the end of the wiggler, the harmonically generated power is less. We will show that when we use the LANL new gun parameters, we are working in the regime similar to the situation in Fig. 3 at about 11 m. For the LANL gun parameters, the subharmonically (100-nm) seeded FEL is superior to the case of a 100-nm seeded FEL.

#### E. Optimization of the parameters

The parameters used in the examples have been optimized. The wiggler period and electron-beam energy have been selected based on the analytical calculation as

explained in Sec. II B. We now elaborate a little further on the optimization of the input laser power, the dispersion strength, the starting position of the tapering, and the percent of tapering of the wiggler field.

The input 300-nm laser power and the optimum dispersion section strength  $d\theta/d\gamma$  are closely related. For fixed laser power, the energy modulation at the exit of the second wiggler is fixed, and there is an optimum dispersion strength for best microbunching and maximum harmonic components. When the input laser power increases and the energy modulation increases, the corresponding harmonic components also increase. Hence increasing the input laser power enhances the harmonic generation in the first 2 m, but the exponential growth rate after the first 2 m drops because of the larger effective energy spread resulting from the increased modulation. Therefore, when we calculate the 100-nm radiation power at 5 m into the second wiggler, for a set of input laser powers and corresponding optimum dispersion strengths, we find there is an optimum input laser power. For the example based on the ATF gun parameters, the laser power is found to be 1.5 MW with a dispersion strength of  $d\theta/d\gamma=0.33$ . With these parameters, the energy modulation (peak to peak) at the end of the first wiggler is  $2\Delta\gamma/\gamma=1.6\times 10^{-3}$ , comparable to energy spread (FWHM) 0.1%.

Next the starting position of the tapering of the second wiggler is varied to maximize the output power for both the 100- and 300-nm seeded cases. If the tapering is started too early, the radiation power is too low so the trapping efficiency into the separatrix is low. But if the tapering is started too late, the exponential growth saturates and eventually the radiation power drops before the tapering starts, so the output power is reduced. Therefore there is an optimum position. In Fig. 9, for the 100-nm seeded case we plot the output versus the starting position of the tapering, with 1.8% tapering at 21 m.

Finally, the percent of tapering  $\eta$  is also varied to find maximum output for both the 100- and 300-nm seeded FEL. Larger tapering gives larger energy extraction from the trapped electrons, but more electrons are de-

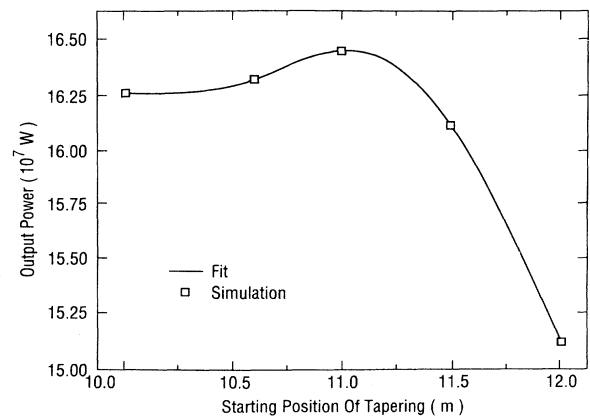


FIG. 9. Output power vs the starting position of the tapering, with 1.8% tapering at 21 m for the 100-nm seed FEL.

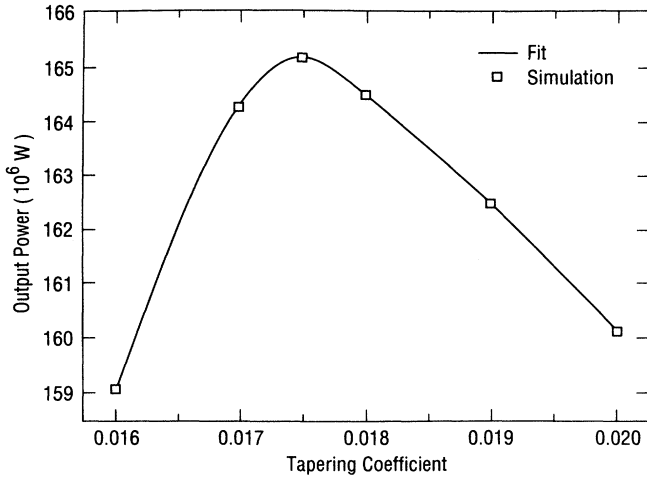


FIG. 10. Phase-space distribution at the end of the tapered section.

trapped, so that even though at the end of the wiggler the bucket has a lower resonant energy, the number of particles in the bucket is small. There is a tradeoff between these two trends. For the ATF parameters, for the 100-nm seeded case, we find the optimum is the starting position at 11 m with a 1.75% tapering at the end of the wiggler. In Fig. 10 we plot the output vs  $\eta$  with the tapering starting position fixed at 11 m. The phase space distribution of electrons and one of the buckets at the end of the tapered section is shown in Fig. 11. This shows that with the optimized parameters, a significant portion of the electrons have leaked out from the bucket at the end. The optimized results for both cases are listed in Table I (columns 1 and 2).

### III. ONE-DIMENSIONAL ANALYTICAL MODEL

To check the simulation, we developed several analytical models. As explained before, the simulation for the exponential regime has been checked against our analyti-

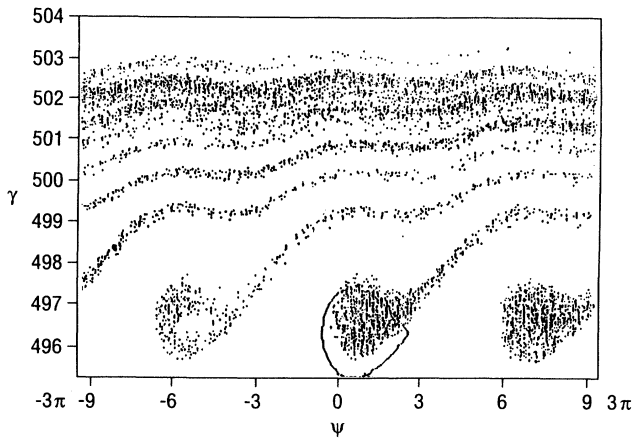


FIG. 11. Output power vs  $\eta$  with the tapering starting position fixed at 11 m for the 100-nm seeded FEL.

cal result with good agreement. This not only tested the code, but also checked our selection of calculated parameters such as the number of simulation particles, the longitudinal step size, the transverse mesh size, etc. The tapered section has been checked with a crude one-dimensional estimate, giving a correct prediction of the length of the exponential section and tapered section to achieve the required power (see Appendix B and Sec. II C). An accurate analytical calculation is difficult. To test the simulation of the harmonic generation and the following exponential growth for small initial energy spread, the one-dimensional problem can be solved analytically. By increasing the electron-beam size and reducing the energy spread until the growth rate approaches the solvable one-dimensional limit, we have checked our modified version of the TDA against the analytical solution. The full test of the exponential section, the one-dimensional test of our modified TDA calculation of harmonic generation, and the one-dimensional estimate of the tapered section, provide a reliable check of the whole simulation process, and a convenient way to estimate the performance before the simulation.

We can solve the problem in the small energy spread limit because in this case only a very small energy modulation is enough to create strong microbunching in the dispersion section. Then, after the first two gain lengths of coherent harmonic generation in the second wiggler, the effective energy spread due to the modulation can be neglected, and the exponential growth rate is the same as without energy spread. The criterion to determine whether the energy spread is small is to compare it with the Pierce parameter  $\rho$  [13,15], defined by

$$(2\rho\gamma_0)^3 = e^2 Z_0 n_0 a_w^2 [JJ]^2 / 2mck_w^2, \quad (3.1)$$

where  $n_0$  is the electron density. In one-dimensional theory, when energy spread is very small, and the detuning is zero, the power exponential growth is proportional to  $\exp(\sqrt{3}\rho k_w z)$ . For both the 100- and 300-nm seed examples, the Pierce parameter in the exponential section is  $\rho = 1.29 \times 10^{-3}$ , comparable to the energy spread. When the energy modulation is comparable or larger than  $\rho$ , the analytical calculation is difficult because the effective energy spread due to the energy modulation has a rather complicated distribution. As can be seen in Fig. 7(a), the period of the modulation is 300 nm, so in the second wiggler it covers three 100-nm periods, each of which has different energy distribution and remains different at the end of the second wiggler (Figs. 8 and 11).

Now let us give the one-dimensional analytical description of this process. First we describe the microbunching process for a beam with a Gaussian energy distribution, and then we proceed to the harmonic radiation generation and the exponential growth for the case with small energy spread.

Suppose that before entering the first wiggler, the electron distribution is Gaussian in energy and uniform in phase  $\theta$

$$f_0(\delta\gamma) = \frac{1}{\sqrt{2\pi}\sigma_\gamma} e^{-\delta\gamma^2/2\sigma_\gamma^2}, \quad (3.2)$$

where  $\delta\gamma \equiv \gamma - \gamma_0$ . At the end of the first wiggler, there is an energy modulation  $\Delta\gamma \sin\theta$ . Then the distribution function at the entrance to the dispersion section is

$$f_0(\delta\gamma - \Delta\gamma \sin\theta). \quad (3.3)$$

After passing through the dispersion section with dispersion strength  $d\theta/d\gamma$ , the electrons of phase  $\theta$  will have a new phase  $\theta + \delta\gamma d\theta/d\gamma + \theta_0$ , as described in Sec. II D. Hence the distribution function becomes

$$f(\gamma, \theta) = f_0 \left[ \delta\gamma - \Delta\gamma \sin \left[ \theta - \frac{d\theta}{d\gamma} \delta\gamma - \theta_0 \right] \right]. \quad (3.4)$$

The integration of this distribution over energy yields the phase distribution, and the Fourier expansion of this function gives the harmonic components of the density modulation converted from the energy modulation [5],

$$\int f(\gamma, \theta) d\gamma = 1 + 2 \sum_{n=1}^{\infty} \exp \left[ -\frac{1}{2} n^2 \sigma_\gamma^2 \left( \frac{d\theta}{d\gamma} \right)^2 \right] \times J_n \left[ -n \Delta\gamma \frac{d\theta}{d\gamma} \right] \text{cosn}(\theta - \theta_0). \quad (3.5)$$

In this expansion, only the third-harmonic component contributes significantly to the 100-nm coherent radiation because the second wiggler is resonant to this wavelength. The other components can be neglected either because they are not resonant (e.g., the fundamental) or produce radiation with much lower intensity and lower growth rate, dominated by the 100-nm radiation, as explained in Sec. II D. Therefore we can consider that there is only the 100-nm density modulation at the entrance of the second wiggler. It is easy to see that its amplitude can also be expressed as twice the value  $|\langle e^{-in\theta_j} \rangle|$ , which is called the bunching factor:

$$\begin{aligned} & \left| \frac{1}{\pi} \int_{-\pi}^{\pi} \text{cosn}(\theta - \theta_0) d\theta \int f(\gamma, \theta) d\gamma \right| \\ &= 2 |\langle e^{-in\theta_j} \rangle| \\ &= 2 \exp \left[ -\frac{1}{2} n^2 \sigma_\gamma^2 \left( \frac{d\theta}{d\gamma} \right)^2 \right] J_n \left[ n \Delta\gamma \frac{d\theta}{d\gamma} \right], \quad (3.6) \end{aligned}$$

where the harmonic number  $n = 3$  in our example, corresponding to 100 nm.

The Bessel function factor represents the microbunching. In its argument, the factor  $\Delta\gamma d\theta/d\gamma$  is the phase shift due to the energy modulation in the dispersion section. If this factor is much smaller than 1, the microbunching would be reduced proportional to its  $n$ th power. Hence  $d\theta/d\gamma$  must be comparable to  $1/\Delta\gamma$ . The first exponential factor shows that the energy spread erases the microbunching when  $\sigma_\gamma d\theta/d\gamma \approx \sigma_\gamma/\Delta\gamma > 1$ , hence the energy modulation must be larger than or equal to the energy spread in order to have large harmonic components.

Therefore, if the energy spread is comparable to the Pierce parameter  $\rho$ , as is the case for our examples, the

energy distribution should be even larger. However, this in turn will reduce the growth rate in the second wiggler, so the optimized value of energy modulation should be comparable to the energy spread. Optimization utilizing computer simulation has confirmed this, as explained in Sec. II E.

Now we consider the FEL process in the second wiggler. In the linear regime, the FEL problem can be formulated as solving the initial value problem for the coupled Vlasov-Maxwell equations, and a detailed discussion can be found, for example, in Ref. [15]. The initial conditions include the input radiation-field strength and the electron distribution at the entrance to the second wiggler. Since we are discussing the harmonic-generation process, we take the input 100-nm power to be zero. If we assume the energy spread is much smaller than  $\rho$ , then the energy modulation can be selected to be comparable to the energy spread, but still much smaller than  $\rho$  [13], so that the equations can be linearized. Therefore we can solve this problem by assuming zero energy spread and a density modulation

$$2 \exp \left[ -\frac{1}{2} n^2 \sigma_\gamma^2 \left( \frac{d\theta}{d\gamma} \right)^2 \right] J_n \left[ n \Delta\gamma \frac{d\theta}{d\gamma} \right]. \quad (3.7)$$

In the following, we present the results of this calculation, leaving a brief description of the derivation to Appendix A. To compare with the simulation, it is convenient to write the solution in the two asymptotic limits:  $\rho k_w \ll 1$  and  $\rho k_w \gg 1$ . They correspond to the superradiance and the exponential growth regimes, respectively. The dimensionless vector potential for the radiation field, as a function of distance  $z$ , is

$$a_s = \begin{cases} 4 A_0 \rho k_w z & (\rho k_w z \ll 1) \\ \frac{2}{3} A_0 e^{\sqrt{3} \rho k_w z} & (\rho k_w z \gg 1) \end{cases} \quad (3.8)$$

where

$$A_0 = \frac{2k_w (\rho\gamma_0)^2 \exp \left[ -\frac{1}{2} n^2 \sigma_\gamma^2 \left( \frac{d\theta}{d\gamma} \right)^2 \right] J_n \left[ n \Delta\gamma \frac{d\theta}{d\gamma} \right]}{k_s a_w [JJ]}. \quad (3.9)$$

In the first superradiance regime, the field grows linearly with  $z$ , so the power grows quadratically. This is because the electron distribution has not changed very much in the short distance, and we can approximate this process as many rigid microbunches, spaced by integral number of wavelengths, radiating coherently. After about one or two gain lengths ( $\rho k_w z > 1$ ), the energy modulation of the electrons induced by the 100-nm radiation becomes important, hence we can no longer consider the microbunches as rigid, and the growth becomes exponential.

The results of Eq. (3.8) have been used to test our modification of the TDA code to include harmonic generation. To test the code, we simulated a situation close to one-dimensional approximation. We started from the set

of parameters used for the 300-nm seeded FEL based on the ATF gun design, as given in Secs. II B and II D, but increased the current and beam cross section proportionally by a factor of 16 so that the current density remained the same as before, but the radiation beam size was sufficiently large to justify neglecting the diffraction. Next, we set the emittance to zero and the fractional energy spread  $\sigma_\gamma/\gamma = 3 \times 10^{-5}$  so that it was much smaller than the Pierce parameter  $\rho$ . Then, to maintain a parallel beam with a finite but longitudinally invariant electron-beam profile for zero emittance, we set the transverse wiggler field to be constant transversely, so that there was no focusing effect. The input 300-nm laser beam was assumed to have very large beam waist and Rayleigh range so that it could be taken as a plane wave. Under these circumstances, the electron-beam energy was taken to be  $\gamma = 502.63$ , the wiggler period 1.75 cm with  $a_w = 1.37$ , and the Pierce parameter  $\rho = 1.29 \times 10^{-3}$ . We adjusted the input laser power such that the energy modulation  $\Delta\gamma = 0.016$  at the end of the first wiggler was comparable to the energy spread  $\sigma_\gamma = 0.015$ , but  $\Delta\gamma/\gamma = 3.2 \times 10^{-5} \ll \rho$ , thus the effective energy spread due to this energy modulation in the second wiggler could be ignored. The dispersion section strength was chosen to be  $d\theta/d\gamma = 30$ , giving the maximum phase shift  $3\Delta\gamma d\theta/d\gamma = 1.44$ , and the phase shift due to energy spread  $3\sigma_\gamma d\theta/d\gamma = 1.35$ . Thus the bunching factor

$$J_3(3\Delta\gamma d\theta/d\gamma) \exp\left[-\frac{1}{2} \left(3\sigma_\gamma \frac{d\theta}{d\gamma}\right)^2\right] = 0.022.$$

With all these provisions, we obtained good agreement with the analytical result Eq. (3.8). In Fig. 12, we plot the logarithm of the on-axis radiation field  $a_s$  (divided by the constant  $A_0$ ) versus the scaled wiggler distance  $\rho k_w z$ , and the one-dimensional (1D) result of Eq. (3.8). In this plot, the superradiance regime is represented by a logarithmic curve and the exponential growth section by a straight line.

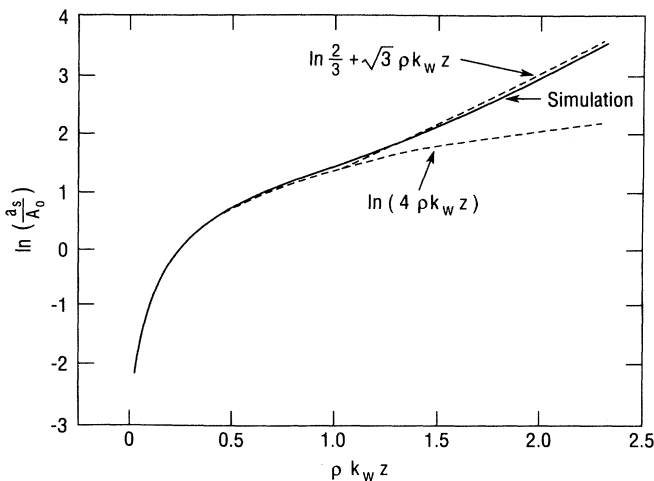


FIG. 12. One-dimensional calculation checked with simulation.

#### IV. A DESIGN EXAMPLE

Now let us consider a design example based on the LANL gun parameters. As explained in the Introduction, we assume an electron pulse length 15 psec from a linear accelerator with a laser driven photocathode rf gun. The electron beam has a peak current of 300 A, normalized emittance (rms) 8 mm mrad, local energy spread 0.1% FWHM, and global energy spread 0.3% (see Table I, column 3). As discussed in Sec. II B, the assumption of 0.1% local energy spread is a conservative estimate. Because the current is higher and the pulse length is longer than what has been discussed in Sec. II B, the wiggler length required to achieve 1-mJ pulse energy becomes much shorter, and we can consider relaxing the requirements on the wigglers. We assume the wiggler is of a SmCo<sub>5</sub> permanent magnet type rather than Nd-Fe-B because it has less temperature dependence and better resistance to radiation damage. The on-axis magnetic field with a 92% contingency factor, is given by Halbach's relation [12]

$$B_w = 0.92(3.16) \exp[-5.47(g/\lambda_w) + 1.8(g/\lambda_w)^2]. \quad (4.1)$$

To reduce the effect of the wake field in the vacuum chamber the wiggler gap is increased from 4 to 6 mm.

The first step of design is to optimize the wiggler period by minimizing the gain length for the exponential section of the second wiggler. Using the analytical method, as discussed in Sec. II B, we find the optimized parameters: wiggler period  $\lambda_{w2} = 2.2$  cm, with maximum on-axis magnetic field  $B_{w2} = 0.75$  T and  $a_{w2} = 1.09$ , electron-beam energy  $\gamma = 490$ , edge beam size  $R_0 = 0.47$  mm, and the power gain length  $L_G = 1.07$  m at 100 nm. Next, the period and magnetic field of the first wiggler (the modulator) are chosen to be resonant to 300 nm, and with approximately the same betatron wavelength. The result gives a wiggler period of  $\lambda_{w1} = 3.5$  cm with  $B_{w1} = 0.76$  T and  $a_{w1} = 1.77$ .

After selecting the wiggler parameters, we optimize the input 300-nm laser power and the dispersion strength by finding the maximum radiation power at a few gain lengths into the second wiggler, in the exponential regime. We assume the first wiggler is 2 m long, then we find optimized laser power to be 4.2 MW, with an optimized dispersion strength  $d\theta/d\gamma = 0.83$ . For a dispersion section of total length of 20 cm, this corresponds to a magnetic field of 2.8 kG. This set of parameters gives an energy modulation  $\Delta\gamma/\gamma = 1.43 \times 10^{-3}$  at the end of the first wiggler. This is comparable to the FWHM energy spread 0.1% and the Pierce parameter  $\rho = 1.53 \times 10^{-3}$ . Because this is equivalent to an energy spread, the power gain length is increased slightly to 1.37 m, as compared with the gain length 1.07 m for electron beam without energy modulation.

Next, based on a one-dimensional estimate, we choose the length of the second wiggler to be 11 m. Then utilizing the modified TDA code we vary the starting position of tapering and the percent of tapering at the end of the wiggler individually, until we find the maximum output

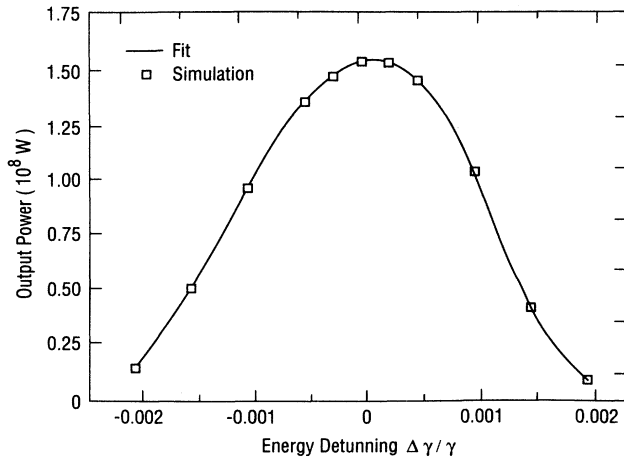


FIG. 13. Output power as a function of energy detuning for the 300-nm seeded FEL with LANL gun parameters.

power. The result is to start tapering at 7 m and to taper 1.2% at the end of the wiggler, with an output power of 155 MW. For a pulse width of 10 psec, this produces 1.55 mJ per pulse. The radiation power versus distance in the second wiggler is plotted in Fig. 2.

Finally, we consider the effect of the global energy spread. Assuming that the average electron energy deviates from the optimum value  $\gamma_0=490$ , but all the other parameters remain fixed, we calculate the output power as a function of this energy detuning. The result is plotted in Fig. 13, with a FWHM width of about 0.25% detuning range. Thus, if the energy fluctuation from bunch to bunch is within 0.25%, the output power would fluctuate between 75 and 155 MW from pulse to pulse. If the energy is stabilized to better than 0.25%, but the energy variation within one bunch is still 0.25%, then the intensity fluctuation between pulses would be reduced, and the energy per pulse would be stabilized around a certain average value between 0.75 and 1.55 mJ for a pulse length of 10 psec. The FWHM energy detuning range for this example and the two previous samples for the ATF gun parameters are listed in Table I.

We have given a description of the principles and calculation of a subharmonically seeded single-pass uv FEL. However, there are still many questions to be addressed before a more detailed design can be carried out. The requirement on the tolerances of the wiggler errors is under study. Using a one-dimensional analytical method [16], we have studied the gain reduction due to longitudinal phase shift caused by wiggler field amplitude error. The analysis shows that in the exponential regime, the rms random phase shift per wiggler period times the square root of the number of period within one gain length determines whether this effect is important. Therefore, when gain length is small, the tolerances on the amplitude error of the wiggler field are relaxed. It also shows that the effects caused by the transverse steering of wiggler error are more critical than the amplitude error. However, steering error can be corrected by trim dipole magnets. Detailed numerical simulation of both longitu-

dinal and transverse effects due to wiggler errors is in progress. A quantitative calculation of the higher harmonics in the second wiggler, which coexist with the fundamental wavelength (100 nm), should be carried out in the future to justify our neglect of them.

In the exponential section, the fundamental mode gradually dominates other modes, so that before tapering the radiation has evolved into single mode, and the beam profile becomes constant (optical guiding). However, in the tapered section, the growth rate becomes smaller, so diffraction starts to increase the radiation beam size. How this influences the transverse coherence of the output radiation is a question worth further study. Other questions to be addressed include: a more detailed simulation of the dispersion section, analysis of the correction magnets to eliminate steering errors, and an analysis of the effect of wake fields in the vacuum chamber.

#### ACKNOWLEDGMENTS

The author has benefited from many discussions with S. Krinsky I. Ben-Zvi, and R. Gluckstern, and also wants to express his gratitude to S. Krinsky for many suggestions and comments on this paper. We specially express our gratitude to J. Wurtele for kindly providing us with the code TDA. We thank J. Goldstein and T. Scharlemann for providing simulation results from the codes FELEX and FRED, respectively. We learned much from discussions with R. Bonifacio, C. Pellegrini, C. M. Tang, and K. J. Kim. We also want to thank A. Friedman, and K. M. Yang for discussions and collaboration on the calculations. This work has been performed under the auspices of the U.S. Department of Energy.

#### APPENDIX A: ONE-DIMENSIONAL ANALYTICAL ANALYSIS OF SUBHARMONICALLY SEEDED HIGH-GAIN FEL

For a detailed formulation of high-gain FEL theory, we refer to one of our earlier papers [15]. With slight modifications to consider a planar wiggler, instead of helical wiggler, we will use the formulation in Ref. [15] to derive the formulas for our one-dimensional analysis of the subharmonically seeded FEL. We start from the Vlasov-Maxwell equations. Let  $E(z, t)$  be the slowly varying envelope function of the electric field:

$$\mathcal{E} = \hat{\mathbf{x}}E \cos(k_s z - \omega_s t) \quad (\text{A1})$$

where  $\hat{\mathbf{x}}$  is the unit vector. The electron distribution function is also expressed by the slowly varying envelope

$$f(\tau, \psi) = F(\tau, \psi, \gamma) e^{i\psi} + \text{c.c.}, \quad (\text{A2})$$

where  $\tau = k_w z$ , and  $\psi = (k_s + k_w)z - \omega_s t$  corresponding to the  $\psi_j$  defined by Eq. (2.21). For simplicity, we neglect the subscript "2" for the wave numbers and the frequency in these formulas, which refers to the second wiggler.

Equations (7.2) and (7.3) of the Ref. [15], the Vlasov-Maxwell equations, can be written as

$$\left[ \frac{\partial}{\partial \tau} + \frac{\partial}{\partial \psi} \right] E = D_1 \int \frac{d\gamma}{\gamma} F, \quad (\text{A3})$$

$$\left[ \frac{\partial}{\partial \tau} + 2 \frac{\gamma - \gamma_0}{\gamma_0} \left[ \frac{\partial}{\partial \psi} + i \right] \right] F = D_2 \frac{1}{\gamma} \frac{\partial f_0}{\partial \gamma} E, \quad (\text{A4})$$

where

$$D_1 = \frac{n_0 \mu_0 e c^2 a_w}{\sqrt{2} k_w} [JJ], \quad (\text{A5})$$

$$D_2 = \frac{e a_w}{2\sqrt{2} m c^2 k_w} [JJ], \quad (\text{A6})$$

with  $\mu_0$  the vacuum magnetic permeability. The initial electron distribution function  $f_0$ , as explained in Ref. [15], is assumed to be monoenergetic and uniform  $f_0 = \delta(\gamma - \gamma_0)$ . The constants  $D_1$  and  $D_2$  are related to the Pierce parameter  $\rho$  by

$$(2\rho)^3 = 2D_1 D_2 / \gamma_0^3. \quad (\text{A7})$$

Because we are considering the one-dimensional problem, the transverse Laplacian in Eqs. (7.2) and (7.3) of Ref. [15] is dropped.

We introduce the Fourier transform over  $\psi$

$$\bar{E}(\tau; q) = \int_{-\infty}^{\infty} d\psi e^{-iq\psi} E(\tau, \psi), \quad (\text{A8})$$

$$\bar{F}(\tau, \gamma; q) = \int_{-\infty}^{\infty} d\psi e^{-iq\psi} F(\tau, \psi, \gamma), \quad (\text{A9})$$

and the Laplace transform over  $\tau$ ,

$$\bar{E}(\Omega, q) = \int_0^{\infty} d\tau e^{i\Omega\tau} \bar{E}(\tau; q), \quad (\text{A10})$$

$$\bar{F}(\gamma; \Omega, q) = \int_0^{\infty} d\tau e^{i\Omega\tau} \bar{F}(\tau, \gamma; q), \quad (\text{A11})$$

where  $\text{Im}\Omega$  is positive and large enough to guarantee convergence of the integral over  $\tau$ . Applying the Fourier-Laplace transform to Eqs. (A3) and (A4) yields

$$(-i\Omega + iq)\bar{E} = D_1 \int d\gamma \frac{1}{\gamma} \bar{F} + \bar{E}(\tau=0), \quad (\text{A12})$$

$$\left[ -i\Omega + i2 \frac{\gamma - \gamma_0}{\gamma_0} (1+q) \right] \bar{F} = D_2 \frac{1}{\gamma} \frac{\partial f_0}{\partial \gamma} \bar{E} + \bar{F}(\tau=0). \quad (\text{A13})$$

We assume the initial value of the radiation field  $\bar{E} = 0$ , and the initial energy-density modulation is monochromatic, with the wavelength resonant to the second wiggler, i.e., we take the detuning of the coherently generated radiation  $q \equiv \delta\omega/\omega = 0$ , hence all the Fourier-transformed functions  $\bar{E}$  and  $\bar{F}$  are proportional to  $\delta(q)$ . If the energy modulation is much smaller than the Pierce parameter  $\rho$ , then we can show that in Eq. (A13),  $\Omega$  is the same order of magnitude as  $\rho$ , and the energy deviation term  $(\gamma - \gamma_0)/\gamma_0$  is much smaller than the other term, so it can be neglected. Now Eq. (A13) is used to solve for  $\bar{F}$  and substituted into Eq. (A12) to solve for  $\bar{E}$ . The solution for  $\bar{E}$  is then inverse Laplace transformed to calculate the Fourier transform  $\bar{E}$  at position  $\tau$ :

$$\bar{E}(\tau; q) = \int_{-\infty + is}^{\infty + is} d\Omega \frac{1}{2\pi} e^{-i\Omega\tau} \bar{E}(\Omega, q), \quad (\text{A14})$$

where  $s$  is a sufficiently large positive number such that the integration path is above all the singular points of  $\bar{E}(\Omega, q)$ . The integral can be carried out around the poles in the complex  $\Omega$  plane. Using the fact that  $f_0$  is a  $\delta$  function and the initial value of  $\bar{F}$  has very small energy modulation around  $\gamma_0$ , these poles are found to be the three roots of the well-known cubic equation for the high-gain FEL:

$$\Omega^3 - q\Omega^2 - (2\rho)^3 = 0. \quad (\text{A15})$$

Then all the integrals involved in this solution can be carried out yielding

$$\bar{E}(\tau, q) = \frac{iD_1}{3\gamma_0} \sum_{j=1}^3 \frac{e^{-i\Omega_j\tau}}{\Omega_j} \int d\gamma \bar{F}(\tau=0, q), \quad (\text{A16})$$

and the inverse Fourier transform yields the field

$$E(\tau) = \frac{iD_1}{3\gamma_0} \sum_{j=1}^3 \frac{e^{-i\Omega_j\tau}}{\Omega_j} \int d\gamma F(\tau=0). \quad (\text{A17})$$

Since the detuning  $q$  is zero, and the Fourier coefficients are all proportional to  $\delta(q)$ ,  $E$  is independent of  $\psi$ , and  $\Omega_j = 2\rho \exp[j(i2\pi/3)]$ ,  $j=1,3$ , are the roots of the cubic equations Eq. (A15) with  $q=0$ . Examining Eq. (A2), we can write

$$\int d\gamma F = \int d\gamma f e^{-i\psi} = \langle e^{-i\psi_j} \rangle, \quad (\text{A18})$$

where

$$\psi_j = (k_{s2} + k_{w2})z - \omega_{s2}t_j \quad (\text{A19})$$

is the phase of the particle  $j$  at the entrance of the second wiggler with  $t_j$  the time of arrival, and the angular bracket is an average over one period of the phase. Now let  $\theta_j$  be the phase referenced to the first wiggler, but also at the entrance of the second wiggler, with the same  $z$  and  $t_j$ ,

$$\theta_j = (k_{s1} + k_{w1})z - \omega_{s1}t_j, \quad (\text{A20})$$

we have

$$\psi_j = \frac{\omega_{s2}}{\omega_{s1}} \theta_j + \theta_0 = n\theta_j + \theta_0, \quad (\text{A21})$$

where  $\theta_0$  is independent of the index  $j$ . Therefore we have

$$\begin{aligned} \left| \int d\gamma F \right| &= |\langle e^{-i\psi_j} \rangle| \\ &= |\langle e^{-in\theta_j} \rangle| \\ &= \exp \left[ -\frac{1}{2} n^2 \sigma_\gamma^2 \left( \frac{d\theta}{d\gamma} \right)^2 \right] J_n \left[ n \Delta\gamma \frac{d\theta}{d\gamma} \right], \end{aligned} \quad (\text{A22})$$

which is the bunching factor in Eq. (3.6). Thus we obtained the field as a function of the wiggler distance  $\tau = \rho k_w z$ :

$$|E(\tau)| = \frac{D_1}{3\gamma_0} \exp \left[ -\frac{1}{2} n^2 \sigma_\gamma^2 \left( \frac{d\theta}{d\gamma} \right)^2 \right] \times J_n \left[ n \Delta\gamma \frac{d\theta}{d\gamma} \right] \left| \sum_{j=1}^3 \frac{e^{-i\Omega_j \tau}}{\Omega_j} \right|. \quad (\text{A23})$$

Finally, it is useful to calculate the asymptotic limits in the exponential growth regime  $\rho k_w z \gg 1$  and the super-radiance regime  $\rho k_w z \ll 1$ . We use the relation

$$D_2 |E| = \frac{k_s}{k_w} a_w \frac{1}{2} [JJ] a_s \quad (\text{A24})$$

to convert the electric-field strength  $E$  to the rms dimensionless vector potential  $a_s$ , and use  $\tau = k_w z$  to derive the results Eq. (3.8) and (3.9).

### APPENDIX B: ANALYTICAL ESTIMATE OF SATURATION AND THE OUTPUT POWER OF THE TAPERED SECTION

To estimate starting position of the tapered section, we need to estimate the saturation of the exponential growth. It is well known that in the small-gain regime, the longitudinal equations of motion of the electrons Eq. (2.1) and (2.2) are the pendulum equations with a pendulum frequency

$$\Omega_s^2 \equiv 2 \frac{k_s}{k_w} \frac{a_s a_w}{\gamma^2} [JJ], \quad (\text{B1})$$

if we use the variable  $k_w z$  as ‘‘time.’’ In the small-gain regime,  $a_s$  is nearly a constant, and so is  $\Omega_s$ , hence the electrons follow approximately the pendulum equations, and rotate in the buckets with frequency  $\Omega_s$ . However, in the exponential regime,  $a_s$ , and  $\Omega_s$  increase exponentially, before the electrons rotate a significant angle in the bucket, and bucket height has increased so much that the rotation in the bucket is negligible. If we use  $\text{Im}(\mu)$  to represent the growth rate, and the radiation field  $a_s$  is proportional to  $\exp(-i\mu k_w z)$ , then the condition for exponential growth is  $\Omega_s \ll \text{Im}(\mu)$ . It is easy to recognize that  $\text{Im}(\mu)$  is related to the power gain length  $L_G$  by  $\text{Im}(\mu) = 1/(2k_w L_G)$ . When  $\Omega_s$  increases to be comparable to  $\text{Im}(\mu)$ , the electrons start to rotate significantly in the bucket and the growth rate starts to decrease and reach saturation. The position of saturation is not a precisely defined position and we define the saturation condition to be when the ratio  $\Omega_s / \text{Im}(\mu) \equiv \alpha$  reaches a certain number of an order of magnitude of 1.

To estimate the radiation power, we relate it to the synchrotron rotation frequency  $\Omega_s$ . The energy loss of the electron beam is converted to the radiation energy. It is proportional to  $a_s^2$ , and hence proportional to  $\Omega_s^4$ . Using energy conservation we find the average fractional energy loss:

$$\left\langle \frac{\gamma - \gamma_0}{\gamma_0} \right\rangle = \frac{\Omega_s^4}{(4\rho)^3}, \quad (\text{B2})$$

where  $\rho$  is the Pierce parameter defined by (3.1). In one-dimensional theory, for zero initial energy spread, near

saturation the fractional energy loss is empirically found to be equal to  $\rho$  [13]. To generalize this, we define the saturation condition as

$$\Omega_s = \alpha \text{Im}(\mu) = \sqrt{88/3} \text{Im}(\mu) \approx 1.6 \text{Im}(\mu). \quad (\text{B3})$$

For the one-dimensional case with zero energy spread we have  $\text{Im}(\mu) = \sqrt{3}\rho$  [13]; inserting this into (B3), we can verify that the fractional energy loss is equal to  $\rho$ .

Now, as an example, we estimate the saturation power for the 100-nm seeded FEL (see Sec. II C). Whether our system can be described by one-dimensional theory is determined by a quantity  $\bar{a} = 2\rho\sqrt{2k_s k_w R_0}$  [15], which is a scaled electron-beam size and is related to the ratio of Rayleigh range of a radiation beam with waist equal to the electron-beam size, over the gain length calculated by 1D theory. In our example,  $\bar{a} \approx 3.5$  is moderately larger than 1, and 1D theory provides a reasonably good estimate. Using  $L_G = 1.1$  m and  $\rho = 1.29 \times 10^{-3}$ , we find  $\text{Im}(\mu) \approx 0.98\rho$ . Then (B3) yields  $\Omega_s = 1.6\rho$  and (B2) yields the fractional energy loss  $0.1\rho$ . Hence the saturation power is estimated from the electron-beam power  $P_e$ :

$$P_{\text{sat}} = 0.1\rho P_e = 0.1 \times (1.29 \times 10^{-3}) \times 250 \text{ MV} \times 100 \text{ A} \approx 3.2 \text{ MW}. \quad (\text{B4})$$

The wiggler length required to reach saturation is then obtained from the following formula, derived for one-dimensional approximation:

$$P = \frac{1}{9} P_{\text{input}} e^{z/L_G}. \quad (\text{B5})$$

When  $L_G$  is accurate, this formula is a good approximation if the input laser focusing is optimized. Substituting  $P_{\text{input}} = 700$  W and  $P = P_{\text{sat}} \approx 3.2$  MW into (B5), we find the exponential growth section length is  $L = 10.6L_G \approx 11.7$  m.

Next, let us estimate the output power of the tapered section. Using the 1D formula Eq. (4.31) of the Ref. [17], given by Kroll, Morton, and Rosenbluth, assuming the resonance phase  $\psi_r$  to be constant and the energy extraction is only a very small fraction of the electron beam, we derived approximately

$$P_{\text{out}} \approx \frac{Z_0}{2\pi} \left[ \frac{e}{mc^2} \right]^2 (f_{\text{trap}} [JJ] \sin\psi_r)^2 \left[ \frac{N_w \lambda_s P_e}{R_0} \right]^2, \quad (\text{B6})$$

where  $N_w$  is the number of periods of the tapered section, and  $f_{\text{trap}}$  is the fraction of the number of electrons trapped in the bucket. In our example, the Rayleigh range of a Gaussian radiation beam with waist equal to the electron-beam radius  $R_0 = 0.3$  mm is  $k_s R_0^2 / 2 = 2.8$  m. If the tapered section is 10 m long, as an estimate we can ignore the diffraction and use the 1D formula. Assuming 50% trapping, and  $\sin\psi_r = 0.5$ , we have

$$P_{\text{out}} \approx 1.4 \times 10^{-11} \left[ \frac{N_w \lambda_s P_e [JJ]}{R_0} \right]^2, \quad (\text{B7})$$

where the electron-beam power  $P_e$  is in units of watts.

For a 10-m tapered section with  $\lambda_w = 1.75$  cm,  $N_w = 571$ , and using the parameters given in Sec. II B,  $R_0 = 0.3$  mm,  $P_e = 250$  MV  $\times$  100 A = 25 GW, and  $\lambda = 10^{-7}$  m, we obtained  $[JJ] = 0.81$  and  $P_{\text{out}} \approx 210$  MW.

In summary, using analytic estimate, we have found that the wiggler should have an 11.7-m exponential growth section and a 10-m tapered section for the 100-nm seeded FEL. Using ATF gun parameters, the estimated

saturation power is 3.2 MW, and the estimated output power is 210 MW. This is to be compared with the simulation for a 21-m wiggler, the optimized tapering starting position is at 11 m, with saturation at 3.2 MW and the output power 160 MW. Considering the rough nature of the analytic estimate, agreement of the output power is good. Analytic estimates are very useful in considering preliminary FEL designs.

- 
- [1] National Synchrotron Light Source Report No. BNL-45499, 1990 (unpublished).
  - [2] I. Ben-Zvi, L. F. Di Mauro, S. Krinsky, M. G. White, and L. H. Yu, Nucl. Instrum. Methods A **304**, 181 (1991).
  - [3] D. W. Feldman *et al.*, Nucl. Instrum. Methods A **304**, 224 (1991).
  - [4] R. Bonifacio, L. De Salvo Souza, P. Pierini, and E. T. Scharlemann, Nucl. Instrum. Methods A **296**, 787 (1990).
  - [5] P. L. Czonka, Part. Accel. **8**, 225 (1978); V. Stagno, G. Brautti, T. Clauser, and I. Boscolo, Nuovo Cimento B **56**, 219 (1980); W. B. Colson, IEEE J. Quantum Electron. **QE-17**, 1417 (1981); R. Coisson and F. DeMartini, *Physics of Quantum Electronics* (Addison-Wesley, Reading, MA, 1982), Vol. 9; P. Elleaume, *ibid.*, Vol. 8.
  - [6] A. Bhowmik, J. Madey, and S. Benson, Nucl. Instrum. Methods A **272**, 183 (1988).
  - [7] L. H. Yu, S. Krinsky, and R. Gluckstern, Phys. Rev. Lett. **64**, 3011 (1990).
  - [8] T. M. Tran and J. S. Wurtele, Comput. Phys. Commun. **54**, 263 (1989).
  - [9] E. T. Scharlemann, J. Appl. Phys. **58**, 2154 (1985).
  - [10] J. Goldstein, T. F. Wang, B. E. Newnam, B. D. McVey, in *Proceedings of the 1987 Particle Accelerator Conference, Washington, DC*, edited by E. R. Lindstrom and L. S. Taylor (IEEE, New York, 1987), p. 202.
  - [11] E. T. Scharlemann and W. M. Fawley, Proc. SPIE Int. Soc. Opt. Eng. **642**, 2 (1986).
  - [12] K. Halbach, J. Phys. (Paris) Colloq. **44**, C1-211 (1983).
  - [13] R. Bonifacio, C. Pellegrini, and L. M. Narducci, Opt. Commun. **50**, 373 (1984).
  - [14] J. C. Gallardo and C. Pellegrini, Nucl. Instrum. Methods A **296**, 448 (1990).
  - [15] S. Krinsky and L. H. Yu, Phys. Rev. A **35**, 3406 (1987).
  - [16] L. H. Yu, S. Krinsky, and R. Gluckstern (unpublished).
  - [17] N. M. Kroll, P. L. Morton, and M. N. Rosenbluth, IEEE J. Quantum Electron. **QE-17**, 1436 (1981).